Available online at www.sciencedirect.com
SCIENCE DIRECT
Journal of Sound and Vibration 295 (2006) 685–707
JOURNAL OF SOUND AND VIBRATION
www.elsevier.com/locate/jsvi

Modeling wave propagation in damped waveguides of arbitrary cross-section

Ivan Bartoli[a,b], Alessandro Marzani[a,b], Francesco Lanza di Scalea[a,*], Erasmo Viola[b]

[a]*NDE & Structural Health Monitoring Laboratory, Department of Structural Engineering, University of California, San Diego, 9500 Gilman Drive, La Jolla, CA 92093-0085, USA*
[b]*Dipartimento di Ingegneria delle Strutture, dei Trasporti, delle Acque, del Rilevamento, del Territorio (DISTART), Universita' degli Studi di Bologna, Via Risorgimento 2, 40136 Bologna, Italia*

Received 13 June 2005; received in revised form 27 December 2005; accepted 14 January 2006
Available online 20 March 2006

Abstract

This paper deals with a semi-analytical finite element (SAFE) method for modeling wave propagation in waveguides of arbitrary cross-section. The method simply requires the finite element discretization of the cross-section of the waveguide, and assumes harmonic motion along the wave propagation direction. The general SAFE technique is extended to account for viscoelastic material damping by allowing for complex stiffness matrices for the material. The dispersive solutions are obtained in terms of phase velocity, group velocity (for undamped media), energy velocity (for damped media), attenuation, and cross-sectional mode shapes. Knowledge of these properties is important in any structural health monitoring attempt that uses ultrasonic guided waves. The proposed SAFE formulation is applied to several examples, including anisotropic viscoelastic layered plates, composite-to-composite adhesive joints and railroad tracks.
© 2006 Elsevier Ltd. All rights reserved.

1. Introduction

Guided ultrasonic waves provide a highly efficient method for the non-destructive evaluation (NDE) and the structural health monitoring (SHM) of solids with finite dimensions. Compared to ultrasonic bulk waves, guided waves provide larger monitoring ranges and the complete coverage of the waveguide cross-section. Compared to global vibrations, guided waves provide increased sensitivity to smaller defects due to the larger frequencies. These advantages can be fully exploited only once the complexities of guided wave propagation are unveiled and managed for the given test structure. These complexities include the existence of multiple modes, the frequency-dependent velocities (dispersion), and the frequency-dependent attenuation. For example, the knowledge of the wave velocity is important for mode identification. Similarly, the knowledge of those mode–frequency combinations propagating with minimum attenuation losses helps maximizing the inspection coverage.

Semi-analytical finite element (SAFE) methods, also referred to in the literature as spectral or waveguide finite element methods, have emerged for modeling the guided wave propagation numerically as an alternative

*Corresponding author. Tel.: +1 858 822 1458; fax: +1 858 534 6373.
E-mail address: flanza@ucsd.edu (F. Lanza di Scalea).

0022-460X/$ - see front matter © 2006 Elsevier Ltd. All rights reserved.
doi:10.1016/j.jsv.2006.01.021

to the "exact" methods based on the superposition of bulk waves—SPBW, that include the popular matrix-based methods [1]. Motivations for the numerical methods include the necessity for modeling a large number of layers such as composite laminates and that of modeling waveguides with arbitrary cross-section for which exact solutions do not generally exist. In addition, when complex wavenumbers are part of the solution such as in the case of leaky and/or damped waveguides, the exact SPBW methods require iterative bi-dimensional root-searching algorithms that may miss some of the solutions [1].

The general SAFE approach for extracting dispersive solutions uses a finite element discretization of the cross-section of the waveguide alone. The displacements along the wave propagation direction are conveniently described in an analytical fashion as harmonic exponential functions. Thus only a bi-dimensional discretization of the cross-section is needed, with considerable computational savings compared to a 3-D discretization of the entire waveguide. The SAFE solutions are obtained in a stable manner from an eigenvalue problem, and thus do not require the root-searching algorithms used in SPBW approaches. In addition, since polynomial approximation of the displacement field along the waveguide is avoided, the method is applicable to predicting waves with very short wavelengths, where a traditional 3-D approximation may fail.

A SAFE method for waveguides of arbitrary cross-section was demonstrated for the first time in 1973 [2,3]. In these works dispersive solutions were obtained for the propagative modes only (i.e. real wavenumbers only). The same technique was used a decade later [4] to calculate both propagative modes and nonpropagative, evanescent modes (complex wavenumbers) for anisotropic cylinders. While the evanescent modes do not transport any energy along the structure, they are important from a theoretical viewpoint to satisfy the boundary conditions. More recently, SAFE methods confined to obtaining the propagative solutions were applied to thin-walled waveguides [5], railroad tracks [6] and wedges [7]. An approximation of the method in Refs. [5,6] was also implemented in a standard finite element package by imposing a cyclic axial symmetry condition [8]. An extension can be found in Ref. [9] which examined waveguides immersed in water. Other versions of the general SAFE method, again for the propagative modes, were applied to nonhomogeneous anisotropic beams [10], rods and rails [11]. Both propagative and evanescent modes in twisted waveguides were studied by SAFE methods in Ref. [12]. Reflection phenomena from the end of a waveguide were studied in Ref. [13]. Modes in built-up thin-walled structures, including a channel beam and a plate in a wind tunnel, were examined in Ref. [14]. In this work an interesting formulation was presented for obtaining the group velocity values from the individual solutions of the SAFE eigenproblem. This is advantageous compared to the incremental calculations that are required in the conventional derivation of the group velocity defined as $c_g = \partial\omega/\partial\xi$ (ω is the frequency and ξ is the wavenumber). Laminated composite waveguides were studied by SAFE methods for the first time in Ref. [15] and, subsequently, in Refs. [16,17] for laminated plates of both finite and infinite widths.

The focus of previous SAFE works was obtaining propagative and evanescent modes in undamped waveguides. A need exists to extend this technique to account for material damping. One very recent work [18] demonstrates a SAFE application to damped, viscoelastic composite laminates. In this reference a damping loss factor was estimated indirectly from the power dissipated by the wave. However, the formulation in Ref. [18] still does not allow for the calculation of the true wave attenuation since the governing stiffness matrix was assumed real. In Ref. [19], another damping loss factor was considered in a complex formulation for the material's Young's modulus. The focus of this reference was on global dynamic behavior of plate systems rather than ultrasonic guided waves.

The present study extends the SAFE method for modeling dispersive solutions in waveguides of arbitrary cross-sections by accounting for material damping. This extension is particularly relevant for NDE/SHM applications on high-loss materials such as viscoelastic fiber-reinforced polymer composites. When accounting for damping, the exact energy velocity, rather than the conventional group velocity, is calculated along with the frequency-dependent attenuation of the modes. Various examples are shown, including isotropic plates, composite laminates, composite-to-composite adhesive joints and railroad tracks.

2. Viscoelastic models for wave propagation

This section reviews the linear viscoelastic models that were used in the SAFE formulation proposed in the present work. As well known, for time harmonic motion $e^{-i\omega t}$, linear viscoelasticity can be modeled by

allowing complex components in the material's stiffness matrix

$$\tilde{\mathbf{C}} = \mathbf{C}' - \mathrm{i}\mathbf{C}'' \tag{1}$$

where $\mathbf{C}'$ contains the storage moduli and $\mathbf{C}''$ contains the loss moduli.

In practice, the matrix $\tilde{\mathbf{C}}$ can be expressed as a combination of the elastic stiffness tensor, $\mathbf{C}$, and the viscosity tensor, $\boldsymbol{\eta}$:

$$\mathbf{C} = \begin{bmatrix} C_{11} & C_{12} & C_{13} & C_{14} & C_{15} & C_{16} \\ & C_{22} & C_{23} & C_{24} & C_{25} & C_{26} \\ & & C_{33} & C_{34} & C_{35} & C_{36} \\ & & & C_{44} & C_{45} & C_{46} \\ & & & & C_{55} & C_{56} \\ \text{Sym.} & & & & & C_{66} \end{bmatrix}, \quad \boldsymbol{\eta} = \begin{bmatrix} \eta_{11} & \eta_{12} & \eta_{13} & \eta_{14} & \eta_{15} & \eta_{16} \\ & \eta_{22} & \eta_{23} & \eta_{24} & \eta_{25} & \eta_{26} \\ & & \eta_{33} & \eta_{34} & \eta_{35} & \eta_{36} \\ & & & \eta_{44} & \eta_{45} & \eta_{46} \\ & & & & \eta_{55} & \eta_{56} \\ \text{Sym.} & & & & & \eta_{66} \end{bmatrix}. \tag{2}$$

The coefficients of the viscosity tensor are typically measured at a single-frequency value, $\overline{f}$ (characterization frequency).

The Kelvin–Voigt model and the hysteretic model, both well-established in ultrasonic NDE, were considered in this study to represent material damping. In the Kelvin–Voigt model [20,21] the imaginary component of the stiffness matrix in Eq. (1) is frequency-dependent as $\mathbf{C}'' = \omega\boldsymbol{\eta}$. The complex stiffness coefficients at a generic frequency, f, can be obtained by opportunely scaling the viscoelastic tensor coefficients that are given at the characterization frequency, $\overline{f}$:

$$\tilde{\mathbf{C}} = \mathbf{C}' - \mathrm{i}\frac{\omega}{\overline{\omega}}\boldsymbol{\eta} = \mathbf{C}' - \mathrm{i}\frac{f}{\overline{f}}\boldsymbol{\eta}. \tag{3}$$

In the hysteretic model [20] the complex component of the stiffness matrix is independent of frequency, thus

$$\tilde{\mathbf{C}} = \mathbf{C}' - \mathrm{i}\boldsymbol{\eta}. \tag{4}$$

As a consequence, the hysteretic stiffness matrix has to be determined only once for the entire frequency range examined.

The wave attenuation, defined as the loss per unit distance traveled, is commonly modeled as proportional to the frequency times the imaginary part of the stiffness matrix $\mathbf{C}''$ [20]. From Eqs. (3)–(4), the attenuation is a quadratic function of the frequency in the case of the Kelvin–Voigt model, and a linear function of the frequency in the case of the hysteretic model. It is also evident that both models predict the same attenuation at the characterization frequency $\overline{f}$. The difference between the models becomes increasingly significant as the working frequency differs from the characterization frequency, with the Kelvin–Voigt model resulting in a smaller attenuation than the hysteretic model below $\overline{f}$, and in a larger attenuation above $\overline{f}$.

3. SAFE mathematical framework

3.1. Problem definition

The mathematical model is presented here for the case of a waveguide immersed in vacuum, as shown in Fig. 1(a). This figure refers to an infinitely wide plate; however, the formulation is applicable to arbitrary cross-sections. The wave propagates along direction x with wavenumber ξ and frequency ω. The cross-section lies in the y–z plane. The waveguide can generally be composed of anisotropic viscoelastic materials. The harmonic displacement, stress and strain field components at each point of the waveguide are expressed by

$$\mathbf{u} = \left[u_x\, u_y\, u_z\right]^{\mathrm{T}}, \quad \boldsymbol{\sigma} = \left[\sigma_x\, \sigma_y\, \sigma_z\, \sigma_{yz}\, \sigma_{xz}\, \sigma_{xy}\right]^{\mathrm{T}}, \quad \boldsymbol{\varepsilon} = \left[\varepsilon_x\, \varepsilon_y\, \varepsilon_z\, \gamma_{yz}\, \gamma_{xz}\, \gamma_{xy}\right]^{\mathrm{T}}. \tag{5–7}$$

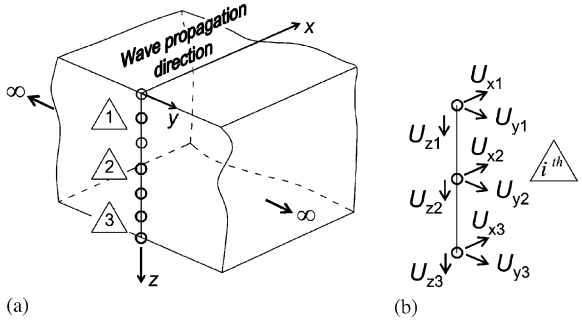

Fig. 1. (a) SAFE model of wave propagation, (b) degrees of freedom of a mono-dimensional three-node element.

The constitutive relations at a point are given by $\boldsymbol{\sigma} = \tilde{\mathbf{C}}\,\boldsymbol{\varepsilon}$, where $\tilde{\mathbf{C}}$ is generally complex as defined in Eq. (1). The compatibility equations can be written in matrix form as

$$\boldsymbol{\varepsilon} = \left[\mathbf{L}_x \frac{\partial}{\partial x} + \mathbf{L}_y \frac{\partial}{\partial y} + \mathbf{L}_z \frac{\partial}{\partial z}\right]\mathbf{u}, \tag{8}$$

where

$$\mathbf{L}_x = \begin{bmatrix} 1 & 0 & 0 \\ 0 & 0 & 0 \\ 0 & 0 & 0 \\ 0 & 0 & 0 \\ 0 & 0 & 1 \\ 0 & 1 & 0 \end{bmatrix}, \quad \mathbf{L}_y = \begin{bmatrix} 0 & 0 & 0 \\ 0 & 1 & 0 \\ 0 & 0 & 0 \\ 0 & 0 & 1 \\ 0 & 0 & 0 \\ 1 & 0 & 0 \end{bmatrix}, \quad \mathbf{L}_z = \begin{bmatrix} 0 & 0 & 0 \\ 0 & 0 & 0 \\ 0 & 0 & 1 \\ 0 & 1 & 0 \\ 1 & 0 & 0 \\ 0 & 0 & 0 \end{bmatrix}. \tag{9}$$

3.2. Equations of motion

Equations of motion for the cross-section are formulated by inserting the kinetic and potential energies into Hamilton's equation. In general, the nonconservative form of Hamilton's principle should be used to account for dissipation. However, the following analysis adopts a simplified approach that assumes a conservative waveguide; the resulting imaginary cross-sectional strain energy distribution is used to estimate the power dissipated by the section via imaginary wavenumbers. The assumption is valid if the cross-sectional strain energy distribution of a propagating wave is not significantly modified by increasing levels of damping [18].

The variation of the Hamiltonian of the waveguide, which vanishes at all material points, is

$$\delta H = \int_{t_1}^{t_2} \delta(\Phi - K)\,\mathrm{d}t = 0, \tag{10}$$

where Φ is the strain energy and K is the kinetic energy. The strain energy is given by

$$\Phi = \frac{1}{2}\int_V \boldsymbol{\varepsilon}^{\mathrm{T}}\tilde{\mathbf{C}}\boldsymbol{\varepsilon}\,\mathrm{d}V, \tag{11}$$

where the upper script T means a transpose vector and V is the volume. The result of this equation is complex: the real component represents the elastic energy, while the imaginary component represents the dissipated energy.

The kinetic energy is given by

$$K = \frac{1}{2}\int_V \dot{\mathbf{u}}^{\mathrm{T}}\rho\dot{\mathbf{u}}\,\mathrm{d}V, \tag{12}$$

where ρ is the mass density and the dot represents a time derivative. By integrating by parts the kinetic term, Eq. (10) can be written as

$$\int_{t_1}^{t_2}\left[\int_V \delta(\boldsymbol{\varepsilon}^{\mathrm{T}})\widetilde{\mathbf{C}}\boldsymbol{\varepsilon}\,\mathrm{d}V + \int_V \delta(\mathbf{u}^{\mathrm{T}})\rho\ddot{\mathbf{u}}\,\mathrm{d}V\right]\mathrm{d}t = 0. \tag{13}$$

The displacement field is assumed harmonic along the propagation direction, x, and spatial functions are used to describe its amplitude in the cross-sectional plane y–z:

$$\mathbf{u}(x,y,z,t) = \begin{bmatrix} u_x(x,y,z,t) \\ u_y(x,y,z,t) \\ u_z(x,y,z,t) \end{bmatrix} = \begin{bmatrix} U_x(y,z) \\ U_y(y,z) \\ U_z(y,z) \end{bmatrix} \mathrm{e}^{\mathrm{i}(\xi x-\omega t)}, \tag{14}$$

where $\mathrm{i} = \mathrm{sqrt}(-1)$ is the imaginary unit.

3.3. Finite element method

The waveguide's cross-sectional domain, Ω, can be represented by a system of finite elements with domain Ω_e. Mono- and bi-dimensional elements were considered in the examples that follow. When mono-dimensional elements were used, an original routine was adopted to discretize Ω. Matlab's "pdetool" and the "GID" software were used for the discretization by bi-dimensional elements [22].

The discretized version of the displacement expressions in Eq. (14) over the element domain can be written in terms of the shape functions, $N_k(y,z)$, and the nodal unknown displacements, (U_{xk}, U_{yk}, U_{zk}), in the x, y and z directions (Fig. 1(b)):

$$\mathbf{u}^{(e)}(x,y,z,t) = \begin{bmatrix} \sum_{k=1}^{n} N_k(y,z)U_{xk} \\ \sum_{k=1}^{n} N_k(y,z)U_{yk} \\ \sum_{k=1}^{n} N_k(y,z)U_{zk} \end{bmatrix}^{(e)} \mathrm{e}^{\mathrm{i}(\xi x-\omega t)} = \mathbf{N}(y,z)\mathbf{q}^{(e)}\mathrm{e}^{\mathrm{i}(\xi x-\omega t)}, \tag{15}$$

where

$$\mathbf{N}(y,z) = \begin{bmatrix} N_1 & & & N_2 & & & \ddots & & & N_n & & \\ & N_1 & & & N_2 & & & \ddots & & & N_n & \\ & & N_1 & & & N_2 & & & \ddots & & & N_n \end{bmatrix}, \tag{16}$$

$$\mathbf{q}^{(e)} = \begin{bmatrix} U_{x1} & U_{y1} & U_{z1} & U_{x2} & U_{y2} & U_{z2} & \cdots & \cdots & \cdots & U_{xn} & U_{yn} & U_{zn} \end{bmatrix}^{\mathrm{T}} \tag{17}$$

and n denotes the number of nodes per element. The strain vector in the element can be represented as a function of the nodal displacements:

$$\boldsymbol{\varepsilon}^{(e)} = \left[\mathbf{L}_x\frac{\partial}{\partial x} + \mathbf{L}_y\frac{\partial}{\partial y} + \mathbf{L}_z\frac{\partial}{\partial z}\right]\mathbf{N}(y,z)\mathbf{q}^{(e)}\mathrm{e}^{\mathrm{i}(\xi x-\omega t)} = (\mathbf{B}_1 + \mathrm{i}\xi\mathbf{B}_2)\mathbf{q}^{(e)}\mathrm{e}^{\mathrm{i}(\xi x-\omega t)}, \tag{18}$$

where $\mathbf{L}$ is given by Eq. (9), $\mathbf{B}_1 = \mathbf{L}_y\mathbf{N}_{,y} + \mathbf{L}_z\mathbf{N}_{,z}$, $\mathbf{B}_2 = \mathbf{L}_x\mathbf{N}$, and $\mathbf{N}_{,y}$ and $\mathbf{N}_{,z}$ are the derivatives of the shape function matrix with respect to the y and z directions, respectively.

Indicating by n_{el} the total number of cross-sectional elements, the discrete form of the Hamilton formulation of Eq. (13) becomes

$$\int_{t_1}^{t_2}\left\{\bigcup_{e=1}^{n_{\mathrm{el}}}\left[\int_{V_e}\delta\left(\boldsymbol{\varepsilon}^{(e)^{\mathrm{T}}}\right)\tilde{\mathbf{C}}_e\boldsymbol{\varepsilon}^{(e)}\,\mathrm{d}V_e+\int_{V_e}\delta\left(\mathbf{u}^{(e)^{\mathrm{T}}}\right)\rho_e\ddot{\mathbf{u}}^{(e)}\,\mathrm{d}V_e\right]\right\}\mathrm{d}t=0, \tag{19}$$

where $\widetilde{\mathbf{C}}_e$ and ρ_e are the element's complex stiffness matrix and density, respectively.

The substitution of Eq. (18) into the strain energy term in Eq. (19), followed by algebraic manipulations, yields

$$\begin{aligned}
&\int_{V_e}\delta\left(\boldsymbol{\varepsilon}^{(e)^{\mathrm{T}}}\right)\widetilde{\mathbf{C}}_e\,\boldsymbol{\varepsilon}^{(e)}\,\mathrm{d}V_e\\
&=\int_{\Omega_e}\int_x\delta\left(\mathbf{q}^{(e)^{\mathrm{T}}}\left(\mathbf{B}_1^{\mathrm{T}}-\mathrm{i}\xi\mathbf{B}_2^{\mathrm{T}}\right)\left[\mathrm{e}^{\mathrm{i}(\xi x-\omega t)}\right]^*\right)\widetilde{\mathbf{C}}_e(\mathbf{B}_1+\mathrm{i}\xi\mathbf{B}_2)\mathbf{q}^{(e)}\mathrm{e}^{\mathrm{i}(\xi x-\omega t)}\,\mathrm{d}x\,\mathrm{d}\Omega_e\\
&=\int_{\Omega_e}\delta\left[\mathbf{q}^{(e)^{\mathrm{T}}}\left(\mathbf{B}_1^{\mathrm{T}}-\mathrm{i}\xi\mathbf{B}_2^{\mathrm{T}}\right)\right]\widetilde{\mathbf{C}}_e(\mathbf{B}_1+\mathrm{i}\xi\mathbf{B}_2)\mathbf{q}^{(e)}\,\mathrm{d}\Omega_e\\
&=\delta\mathbf{q}^{(e)^{\mathrm{T}}}\int_{\Omega_e}\left[\mathbf{B}_1^{\mathrm{T}}\widetilde{\mathbf{C}}_e\mathbf{B}_1-\mathrm{i}\xi\mathbf{B}_2^{\mathrm{T}}\widetilde{\mathbf{C}}_e\mathbf{B}_1+\mathrm{i}\xi\mathbf{B}_1^{\mathrm{T}}\widetilde{\mathbf{C}}_e\mathbf{B}_2+\xi^2\mathbf{B}_2^{\mathrm{T}}\widetilde{\mathbf{C}}_e\mathbf{B}_2\right]\mathrm{d}\Omega_e\mathbf{q}^{(e)},
\end{aligned} \tag{20}$$

where ()* indicates complex conjugate and $\mathrm{i}^{\mathrm{T}}=-\mathrm{i}$. Thus the element stiffness matrix can be calculated by integrating over the cross-sectional domain Ω_e only, since the integration over x reduces to a unity factor due to the complex conjugate terms $\mathrm{e}^{\pm\mathrm{i}(\xi x-\omega t)}$. For viscoelastic materials, the strain energy defined by Eq. (20) consists of a real component, describing the time-averaged elastic energy in the section, and an imaginary component, related to the time-averaged power dissipated by the section.

As for the element kinetic energy contribution in Eq. (19), by using the displacement expressions of Eq. (15) and simplifying the harmonic terms $\mathrm{e}^{\pm\mathrm{i}(\xi x-\omega t)}$, the following can be written

$$\int_{V_e}\delta\left(\mathbf{u}^{(e)^{\mathrm{T}}}\right)\rho_e\ddot{\mathbf{u}}^{(e)}\,\mathrm{d}V_e=\int_{\Omega_e}\int_x\delta\left(\mathbf{u}^{(e)^{\mathrm{T}}}\right)\rho_e\ddot{\mathbf{u}}^{(e)}\,\mathrm{d}x\,\mathrm{d}\Omega_e=-\omega^2\delta\mathbf{q}^{(e)^{\mathrm{T}}}\int_{\Omega_e}\mathbf{N}^{\mathrm{T}}\rho_e\mathbf{N}\,\mathrm{d}\Omega_e\mathbf{q}^{(e)}. \tag{21}$$

Substituting Eqs. (20)–(21) into Eq. (19) yields

$$\int_{t_1}^{t_2}\left\{\bigcup_{e=1}^{n_{\mathrm{el}}}\delta\mathbf{q}^{(e)^{\mathrm{T}}}\left[\mathbf{k}_1^{(e)}+\mathrm{i}\xi\mathbf{k}_2^{(e)}+\xi^2\mathbf{k}_3^{(e)}-\omega^2\mathbf{m}^{(e)}\right]\mathbf{q}^{(e)}\right\}\mathrm{d}t=0, \tag{22}$$

where

$$\begin{aligned}
\mathbf{k}_1^{(e)}&=\int_{\Omega_e}\left[\mathbf{B}_1^{\mathrm{T}}\widetilde{\mathbf{C}}_e\mathbf{B}_1\right]\mathrm{d}\Omega_e,\quad \mathbf{k}_2^{(e)}=\int_{\Omega_e}\left[\mathbf{B}_1^{\mathrm{T}}\widetilde{\mathbf{C}}_e\mathbf{B}_2-\mathbf{B}_2^{\mathrm{T}}\widetilde{\mathbf{C}}_e\mathbf{B}_1\right]\mathrm{d}\Omega_e,\\
\mathbf{k}_3^{(e)}&=\int_{\Omega_e}\left[\mathbf{B}_2^{\mathrm{T}}\widetilde{\mathbf{C}}_e\mathbf{B}_2\right]\mathrm{d}\Omega_e,\quad \mathbf{m}^{(e)}=\int_{\Omega_e}\mathbf{N}^{\mathrm{T}}\rho_e\mathbf{N}\,\mathrm{d}\Omega_e.
\end{aligned} \tag{23}$$

Applying to Eq. (22) standard finite element assembling procedures:

$$\int_{t_1}^{t_2}\left\{\delta\mathbf{U}^{\mathrm{T}}\left[\mathbf{K}_1+\mathrm{i}\xi\mathbf{K}_2+\xi^2\mathbf{K}_3-\omega^2\mathbf{M}\right]\mathbf{U}\right\}\mathrm{d}t=0, \tag{24}$$

where $\mathbf{U}$ is the global vector of unknown nodal displacements, and

$$\mathbf{K}_1=\bigcup_{e=1}^{n_{\mathrm{el}}}\mathbf{k}_1^{(e)},\quad \mathbf{K}_2=\bigcup_{e=1}^{n_{\mathrm{el}}}\mathbf{k}_2^{(e)},\quad \mathbf{K}_3=\bigcup_{e=1}^{n_{\mathrm{el}}}\mathbf{k}_3^{(e)},\quad \mathbf{M}=\bigcup_{e=1}^{n_{\mathrm{el}}}\mathbf{m}^{(e)}. \tag{25}$$

Due to the arbitrariness of $\delta\mathbf{U}$, the following homogeneous general wave equation is finally obtained

$$\left[\mathbf{K}_1+\mathrm{i}\xi\mathbf{K}_2+\xi^2\mathbf{K}_3-\omega^2\mathbf{M}\right]_M\mathbf{U}=0, \tag{26}$$

where the subscript M is the number of total degrees of freedom (dof) of the system.

3.4. Properties of the matrices

The stiffness matrices $\mathbf{K}_1$ and $\mathbf{K}_3$ in Eq. (26) are symmetric, while $\mathbf{K}_2$ is skew symmetric when undamped motion is considered. For damped motion, the $\mathbf{K}_i$ are all generally complex. The "mass" matrix, $\mathbf{M}$, is real symmetric and positive definite regardless of the type of motion (undamped or damped).

$\mathbf{K}_1$ is related to the strain-transformation matrix $\mathbf{B}_1$ that pertains to generalized planar deformations, and thus describes the generalized plane strain behavior or cross-sectional warpage. $\mathbf{K}_3$ models the out-of-plane deformation behavior since it depends on the matrix $\mathbf{B}_2$. $\mathbf{K}_2$ contains both $\mathbf{B}_1$ and $\mathbf{B}_2$ and thus couples the cross-sectional warpage to the out-of-plane deformations.

Without loss of generality, an $M \times M$ transformation diagonal matrix $\mathbf{T}$ is introduced to eliminate the imaginary unit in Eq. (26). The elements of $\mathbf{T}$ corresponding to the u_y and u_z displacement components are equal to 1, while those corresponding to u_x are equal to the imaginary unit:

$$\mathbf{T} = \begin{bmatrix} i & & & & & & \\ & 1 & & & & & \\ & & 1 & & & & \\ & & & \ddots & & & \\ & & & & i & & \\ & & & & & 1 & \\ & & & & & & 1 \end{bmatrix}. \tag{27}$$

This matrix has the properties $\mathbf{T}^{\mathrm{T}} = \mathbf{T}^{*}$ and $\mathbf{T}^{*}\mathbf{T} = \mathbf{T}\mathbf{T}^{*} = \mathbf{I}$, where $\mathbf{I}$ is the identity matrix. The terms in Eq. (26) are pre-multiplied by $\mathbf{T}^{\mathrm{T}}$ and post-multiplied by $\mathbf{T}$. This manipulation does not alter the matrices $\mathbf{K}_1$, $\mathbf{K}_3$ and $\mathbf{M}$ since they do not mix u_x with u_y or u_z:

$$\mathbf{T}^{\mathrm{T}}\mathbf{K}_1\mathbf{T} = \mathbf{K}_1, \quad \mathbf{T}^{\mathrm{T}}\mathbf{K}_3\mathbf{T} = \mathbf{K}_3, \quad \mathbf{T}^{\mathrm{T}}\mathbf{M}\mathbf{T} = \mathbf{M}. \tag{28}$$

The matrix $\mathbf{K}_2$, instead, mixes u_x with u_y and u_z but it does not mix u_y and u_z with each other. It follows that

$$\mathbf{T}^{\mathrm{T}}\mathbf{K}_2\mathbf{T} = -\mathrm{i}\hat{\mathbf{K}}_2, \tag{29}$$

where $\hat{\mathbf{K}}_2$ is a symmetric matrix for undamped motion. The introduction of the matrix T is equivalent to multiplying u_x by the imaginary unit to force the quadrature with u_y and u_z as done in previous works [5,6].

The final form of the eigenvalue problem in Eq. (26) is

$$\left[\mathbf{K}_1 + \xi\hat{\mathbf{K}}_2 + \xi^2\mathbf{K}_3 - \omega^2\mathbf{M}\right]_M \hat{\mathbf{U}} = 0, \tag{30}$$

where $\hat{\mathbf{U}}$ is a new nodal displacement vector. Nontrivial solutions can be found by solving a twin-parameter generalized eigenproblem in ξ and ω. The frequency ω is a real positive quantity. The wavenumber ξ can be either real or complex and can have both positive and negative signs.

3.5. Solutions for undamped media

For lossless materials the stress–strain relation is governed by a real stiffness matrix $\mathbf{C}$. The use of the operator $\mathbf{T}$ is particularly useful in this case since it simplifies Eq. (30) to a real and symmetric system. By assigning real values to ξ, Eq. (30) can be solved as a standard eigenvalue problem in $\omega(\xi)$. All the solutions for this case correspond to propagative waves. Thus if the dimension of the system is equal to M, for each wavenumber ξ_m, M propagating modes (ξ_m, ω_m) are found along with the $\hat{\mathbf{U}}_m$ cross-sectional wavestructure or mode shape.

If the full complex spectrum for both propagative and evanescent modes is of interest, the unknown complex wavenumbers $\xi(\omega)$ must be obtained for a given frequency ω, solving Eq. (30) as a second-order polynomial eigenvalue problem. The resulting complex wavenumbers $\xi = \xi_{\mathrm{Re}} + \mathrm{i}\xi_{\mathrm{Im}}$ are used to describe the velocity of the traveling waves through their real part, ξ_{Re}, and their amplitude decay through the imaginary part, ξ_{Im}. A classic technique to solve the eigenvalue problem $\xi(\omega)$ consists of recasting Eq. (30) to a first-order

eigensystem by doubling its algebraic size

$$[\mathbf{A} - \xi\mathbf{B}]_{2M}\mathbf{Q} = \mathbf{0}, \tag{31}$$

where

$$\mathbf{A} = \begin{bmatrix} \mathbf{0} & \mathbf{K}_1 - \omega^2\mathbf{M} \\ \mathbf{K}_1 - \omega^2\mathbf{M} & \hat{\mathbf{K}}_2 \end{bmatrix}, \quad \mathbf{B} = \begin{bmatrix} \mathbf{K}_1 - \omega^2\mathbf{M} & \mathbf{0} \\ \mathbf{0} & -\mathbf{K}_3 \end{bmatrix}, \quad \mathbf{Q} = \begin{bmatrix} \hat{\mathbf{U}} \\ \xi\hat{\mathbf{U}} \end{bmatrix}. \tag{32}$$

A and **B** are real symmetric matrices. From Eq. (31), at each frequency ω, $2M$ eigenvalues ξ_m and, consequently, $2M$ eigenvectors are obtained. The eigenvectors are the M forward and the corresponding M backward modes. The eigenvalues occur as pairs of real numbers ($\pm\xi_{\mathrm{Re}}$), representing propagative waves in the $\pm x$ directions, as pairs of complex conjugate numbers ($\pm\xi_{\mathrm{Re}} \pm \mathrm{i}\xi_{\mathrm{Im}}$), representing evanescent waves decaying in the $\pm x$ directions, or as pairs of purely imaginary numbers ($\pm\mathrm{i}\xi_{\mathrm{Im}}$), representing the nonoscillating evanescent waves in the $\pm$ x directions. The phase velocity can be then evaluated by $c_{\mathrm{ph}} = \omega/\xi_{\mathrm{real}}$ and the attenuation, in Nepers per meter, by ξ_{Im}.

It should be pointed out that if only the propagative modes in undamped waveguides are of interest, Eq. (30) remains the preferred formulation, since it gives a stable numerical problem and it can be evaluated roughly one hundred times faster that the linearized version in Eq. (31).

In the undamped case, the waves which are nonoscillating evanescent at low frequencies (i.e. purely imaginary wavenumbers) become propagative (i.e. purely real wavenumbers) above their cut-off frequencies, ω_c. The cut-off frequencies can be computed by letting $\xi = 0$ in Eq. (30) and solving the eigenvalue problem

$$\left[\mathbf{K}_1 - \omega_c^2\mathbf{M}\right]_M\hat{\mathbf{U}} = 0. \tag{33}$$

3.6. Solutions for damped media

When material damping is considered, the stiffness matrix $\widetilde{\mathbf{C}}$ is complex according to Eq. (1) and, consequently, the matrices in Eqs. (30) and (31) are also complex. In this case the eigenvalue problem can only be solved for a given frequency in the $\xi(\omega)$ manner from Eq. (31). Since **A** and **B** are now complex, $2M$ complex eigenvalues ξ_m and, consequently, $2M$ complex eigenvectors are obtained for each input frequency ω. In this case there is no analytical distinction between propagative and evanescent modes due to the fact that both types are now represented by complex wavenumbers.

If a Kelvin–Voigt model is used, $\widetilde{\mathbf{C}}$ needs to be scaled in accordance with Eq. (3) considering the characterization frequency $\overline{f}$. Thus this matrix must be updated at each iteration over the frequency domain of interest. In the case of a hysteretic model, instead, $\widetilde{\mathbf{C}}$ can simply be set at the beginning of the simulation for the entire frequency domain.

3.7. Group and energy velocity

In order to compute the group velocity by the conventional manner, the derivatives of the frequency–wavenumber dispersion relations must be calculated based on the differences of the values for adjacent points of the same mode, A and B, i.e. $c_g = \partial\omega/\partial\xi \simeq (\omega_B - \omega_A)/(\xi_B - \xi_A)$. This implies that the accuracy of the velocity solution is sensitive to that of the (ξ, ω) solutions. Also, in this case the (ξ, ω) solutions must be categorized for the different modes (mode tracking). Tracking the modes is not straightforward when one mode approaches another. One technique to track the same mode consists of monitoring the cross-sectional mode shapes in proximity of the overlap between two modes [23]. A method that avoids the necessity for tracking the modes was proposed in Ref. [11]; however, in this work the group velocity accuracy remains dependent on the resolution of the frequency steps.

The necessity for mode tracking, as well as the dependency on the frequency step resolution, can be avoided by calculating the group velocity directly at each (ξ, ω) solution point without any contribution from adjacent points. This approach, recently proposed in Refs. [14,24], was used for the results presented here relative to

undamped waveguides. The procedure starts by evaluating the derivative of Eq. (30) with respect to the wavenumber:

$$\frac{\partial}{\partial \xi}\left(\left[\mathbf{K}(\xi)-\omega^2\mathbf{M}\right]\hat{\mathbf{U}}_R\right)=0, \tag{34}$$

where $\mathbf{K}(\xi)=\mathbf{K}_1+\xi\hat{\mathbf{K}}_2+\xi^2\mathbf{K}_3$ and $\hat{\mathbf{U}}_R$ represents the right eigenvector. Pre-multiplying Eq. (34) by the transpose of the left eigenvector, $\hat{\mathbf{U}}_L^{\mathrm{T}}$:

$$\hat{\mathbf{U}}_L^{\mathrm{T}}\left[\frac{\partial}{\partial \xi}\mathbf{K}(\xi)-2\omega\frac{\partial \omega}{\partial \xi}\mathbf{M}\right]\hat{\mathbf{U}}_R=0. \tag{35}$$

Since $\partial\omega/\partial\xi$ is a scalar, the group velocity can be now written as

$$c_g=\frac{\partial \omega}{\partial \xi}=\frac{\hat{\mathbf{U}}_L^{\mathrm{T}}\left(\hat{\mathbf{K}}_2+2\xi\mathbf{K}_3\right)\hat{\mathbf{U}}_R}{2\omega\hat{\mathbf{U}}_L^{\mathrm{T}}\mathbf{M}\hat{\mathbf{U}}_R}. \tag{36}$$

From this relation the group velocity can be evaluated for each individual solution (ω,ξ) of the dispersion relations at a time independently of any adjacent solution.

As reported in Refs. [25,26], the group velocity definition is not valid in damped waveguides. In this case the wavenumber become complex and the differentiation $c_g=\partial\omega/\partial\xi$ is no longer possible. If the differentiation is made with respect to the real part of the complex wavenumber, then the group velocity calculation yields nonphysical solutions such as infinite velocities at some locations of the dispersion curves. The energy velocity, V_e, is the appropriate property for damped media. The definition of the energy velocity can be found in classical textbooks [27]. The expression used in the present work is

$$V_e=\frac{\frac{1}{\Omega}\int_\Omega \mathbf{P}\cdot\hat{\mathbf{x}}\,\mathrm{d}\Omega}{\frac{1}{T}\int_T\left(\frac{1}{\Omega}\int_\Omega e_{\mathrm{tot}}\,\mathrm{d}\Omega\right)\mathrm{d}t}, \tag{37}$$

where $\hat{\mathbf{x}}$ is the unit vector along the wave propagation direction, $1/T\int_T(..)\,\mathrm{d}t$ denotes the time average over one period T, e_{tot} is the total energy density (kinetic and potential), and $\mathbf{P}$ represents the time averaged Poynting vector (real part only). The time-averaged Poynting vector can be calculated from

$$\mathbf{P}=-\frac{1}{2}\mathrm{Re}(\boldsymbol{\sigma}\dot{\mathbf{u}}^*), \tag{38}$$

where $\boldsymbol{\sigma}$ is the classical 3×3 stress tensor, and $\dot{\mathbf{u}}^*$ is the complex conjugate of the particle velocity vector. The numerator in Eq. (37) is the average power flow carried by a mode in the wave propagation direction over a unit period of time.

The denominator in Eq. (37) can be evaluated by introducing the expressions of the time-averaged energy for the kinetic component, $\langle e_k\rangle_t$, and the potential component, $\langle e_p\rangle_t$, following the formulation in Ref. [20]:

$$\langle e_k\rangle_t=\frac{\omega^2}{4}\rho\mathbf{u}^{\mathrm{T}}\mathbf{u},\quad \langle e_p\rangle_t=\frac{1}{4}\boldsymbol{\varepsilon}^{\mathrm{T}}\mathbf{C}'\boldsymbol{\varepsilon}, \tag{39,40}$$

where the constants $\frac{1}{4}$ result from the time integration over the period T. Eqs. (39) and (40) can be evaluated once the element nodal displacements are calculated from the eigenvalue problem in Eq. (31), and the displacement and strain fields are then reconstructed from Eqs. (15) and (18), respectively.

4. Results

4.1. Plate systems

The general plate system consists of an arbitrary number n of orthotropic layers stacked along the z direction (Fig. 1(a)). The origin of the reference Cartesian system (x, y, z) is located at the top of the layered plate and each layer lies parallel to the x–y plane. The plates considered in this study have an infinite length in the width direction, y. Thus the 2-D cross-section that needs to be interpolated by finite elements reduces to a single line through the plate thickness (Fig. 1). Mono-dimensional quadratic elements were used for the line discretization.

In general, each element can have 3 dof per node, associated to the displacements u_x, u_y and u_z. For isotropic plates, the Lamb modes polarized in the x–z plane are de-coupled from the shear horizontal (SH) modes that are, instead, polarized in the x–y plane. The de-coupling holds for orthotropic plates when the wave propagation direction is along a direction of principal material symmetry. Consequently, in these cases the number of dof of each analysis can be reduced by solving for the Lamb modes and for the SH modes separately (thus considering only u_x and u_z for the former modes, and only u_y for the latter modes). For orthotropic plates with an arbitrary wave propagation direction or for laminated composite plates, the Lamb and the SH modes are coupled and thus these solutions must be found simultaneously.

The mesh refinement used in all of the examples that follow was determined after convergence studies for the dispersive solutions in the frequency range of interest. Clearly, frequencies higher that those examined would require more refined meshes.

4.1.1. Viscoelastic isotropic plate

The first system examined is a viscoelastic isotropic high performance polyethylene (HPPE) plate in vacuum. This plastic material has a relatively high damping. This example was chosen because it was fully studied in Refs. [25,26] by using the software DISPERSE that is based on a SPBW method. The physical and geometric characteristic of the HPPE plate are the same as those in Refs. [25,26]: density $\rho = 953\,\mathrm{kg/m^3}$, thickness $h = 12.7\,\mathrm{mm}$, longitudinal bulk velocity $c_L = 2344\,\mathrm{m/s}$, shear bulk velocity $c_T = 953\,\mathrm{m/s}$, longitudinal bulk wave attenuation $\kappa_L = 0.055\,\mathrm{Np/wavelength}$ and shear bulk wave attenuation $\kappa_T = 0.286\,\mathrm{Np/wavelength}$.

For the SAFE modeling, the complex bulk velocities for the viscoelastic material must be first calculated as

$$\tilde{c}_{L,T} = c_{L,T}\left(1 + i\frac{\kappa_{L,T}}{2\pi}\right)^{-1}. \tag{41}$$

The complex Young's modulus, $\widetilde{E}$, and Poisson's ratio, $\widetilde{\nu}$, can be obtained as

$$\widetilde{E} = \rho\widetilde{c_T}^2\left(\frac{3\widetilde{c_L}^2 - 4\widetilde{c_T}^2}{\widetilde{c_L}^2 - \widetilde{c_T}^2}\right), \quad \widetilde{\nu} = \frac{1}{2}\left(\frac{\widetilde{c_L}^2 - 2\widetilde{c_T}^2}{\widetilde{c_L}^2 - \widetilde{c_T}^2}\right). \tag{42}$$

The complex Lame' constants can be calculated as

$$\widetilde{\lambda} = \frac{\widetilde{E}\widetilde{\nu}}{(1+\widetilde{\nu})(1-2\widetilde{\nu})}, \quad \widetilde{\mu} = \frac{\widetilde{E}}{2(1+\widetilde{\nu})}. \tag{43}$$

Finally, the complex viscoelastic stiffness matrix is given by

$$\widetilde{C} = \begin{bmatrix} \widetilde{\lambda}+2\widetilde{\mu} & \widetilde{\lambda} & \widetilde{\lambda} & & & \\ \widetilde{\lambda} & \widetilde{\lambda}+2\widetilde{\mu} & \widetilde{\lambda} & & & \\ \widetilde{\lambda} & \widetilde{\lambda} & \widetilde{\lambda}+2\widetilde{\mu} & & & \\ & & & \widetilde{\mu} & & \\ & & & & \widetilde{\mu} & \\ & & & & & \widetilde{\mu} \end{bmatrix}. \tag{44}$$

In this case the viscoelastic stiffness matrix is based on the complex bulk wave velocities that are kept constant throughout the frequency range examined. Consequently $\widetilde{\mathbf{C}}$ is independent of frequency and needs to be defined only once at the beginning of the analysis. This procedure is equivalent to an assumption of a hysteretic viscoelastic model.

Forty, quadratic mono-dimensional elements, Fig. 1(b), were used for the SAFE discretization. For the Lamb wave solutions, only the u_x and u_z dof were used. These corresponded to 162 of the total $[n_{\mathrm{el}} \times (n_n - 1) + 1] \times n_{\mathrm{dof}} = 243$ dof. In the previous equation n_{el} is the number of finite elements, $n_n = 3$ is the number of nodes per element and n_{dof} is the number of dof per node.

The resulting Lamb wave solutions are shown in Figs. 2(a)–(d). The energy velocity values, Fig. 2(b), were obtained from Eq. (37). The attenuation values are shown up to 500 Np/m in Fig. 2(c) and up to 3500 Np/m in

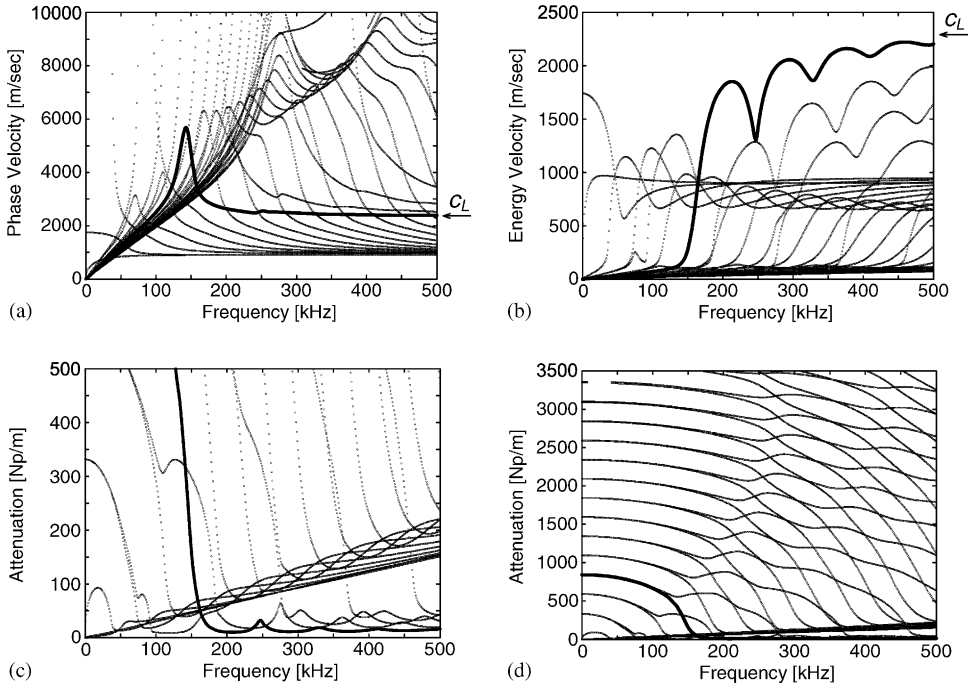

Fig. 2. Dispersion results (Lamb modes) for a 12.7 mm thick, viscoelastic HPPE plate in vacuum: (a) phase velocity, (b) energy velocity, (c) attenuation below 500 Np/m, (d) attenuation below 3500 Np/m. ——, Low-attenuation symmetric mode m.

Fig. 2(d). The frequency range presented is coincident with the one considered in Refs. [25,26]. In these references, however, some of the solutions of the attenuation curves are missing resulting in interrupted or discontinuous branches. This is a consequence of the difficulty of the searching algorithm based on the SPBW method to converge. The SAFE results in Fig. 2 show no missing roots.

Compared to an undamped elastic plate where no solutions exist below the cut-off frequencies, all modes in Fig. 2 have solutions that extend to the origin of the frequency axis. This is the result of the real wavenumber that is now associated to the formerly nonpropagative roots of the undamped case. Below the undamped cut-off frequencies, the damped solutions are characterized by large attenuation values and small energy velocity values. Although these portions have an interesting theoretical significance, they have little practical use in NDE/SHM. If needed, the "nonpropagative" branches can be easily deleted from the dispersion curves by thresholding either the attenuation or the energy velocity values.

Highlighted in Fig. 2 is the symmetric mode, m, that has the lowest attenuation above 165 kHz. Because of the low attenuation, this mode was examined in detail in Ref. [25]. As confirmed in this reference, both phase and energy velocities for m tend to the bulk longitudinal velocity as the frequency increases, since the dominant displacements are along the wave propagation direction.

SAFE solutions for the SH modes are presented in Fig. 3. In this case only 81 dof, corresponding to the u_y displacements, were used in the model. SH modes were not presented in Refs. [25,26], and thus no comparison was possible. All SH solutions are found in the frequency range examined. As expected, the velocities now tend to the shear bulk wave velocity at high frequencies. As found for the Lamb modes, the "nonpropagative" SH modes (i.e. below the undamped cut-off frequencies) have large attenuation values and small energy velocity values.

4.1.2. Elastic transversely isotropic plate

This example examines a 1-mm-thick, unidirectional laminate made of 32, T300/914 carbon-epoxy laminae. The material is considered elastic (undamped). This case was previously studied by using the DISPERSE software based on the SPBW method [23]. The material density is $\rho = 1560\,\mathrm{kg/m^3}$ and the elastic properties in the principal directions of material symmetry are given in Table 1, where 1 is the fiber direction, 2 is the

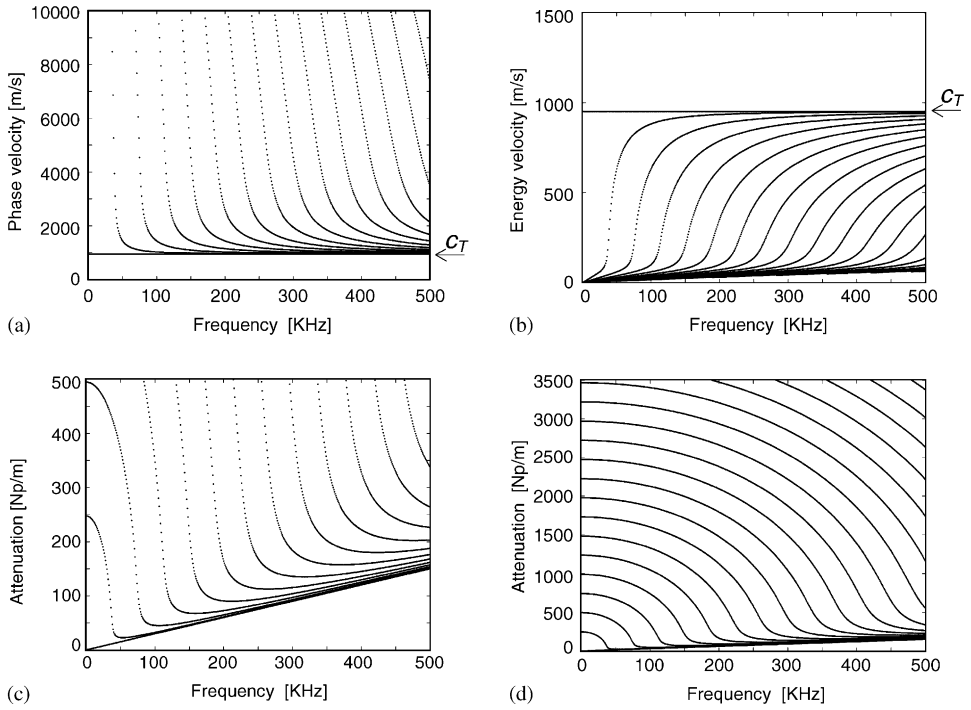

Fig. 3. Dispersion results (SH modes) for a 12.7 mm thick, viscoelastic HPPE plate in vacuum: (a) phase velocity, (b) energy velocity, (c) attenuation up to 500 Np/m, (d) attenuation up to 3500 Np/m.

Table 1
Elastic properties for the T300/914 laminate examined in Ref. [23] and in the present study (elastic constants in GPa)

C_{11}	C_{12}	C_{13}	C_{22}	C_{23}	C_{33}	C_{44}	C_{55}	C_{66}
143.8	6.2	6.2	13.3	6.5	13.3	3.6	5.7	5.7

direction perpendicular to the fibers in the laminate plane, and 3 is the through-thickness direction. The laminate can thus be treated as transversely isotropic, with five independent elastic constants remembering that

$$C_{44} = 0.5 \times (C_{33} - C_{12}). \tag{45}$$

For waves propagating along a direction x oriented at any angle θ with respect to the fiber direction 1, the SAFE model simply requires the rotation of the stiffness matrix of each lamina through

$$\mathbf{C}_\theta = \mathbf{R}_1 \mathbf{C} \mathbf{R}_2^{-1}, \tag{46}$$

where $\mathbf{C}$ is the stiffness matrix in the lamina's principal directions (that can generally be complex), and $\mathbf{R}_1$ and $\mathbf{R}_2$ are the rotation matrices

$$\mathbf{R}_1 = \begin{bmatrix} m^2 & n^2 & 0 & 0 & 0 & 2mn \\ n^2 & m^2 & 0 & 0 & 0 & -2mn \\ 0 & 0 & 1 & 0 & 0 & 0 \\ 0 & 0 & 0 & m & -n & 0 \\ 0 & 0 & 0 & n & m & 0 \\ -mn & mn & 0 & 0 & 0 & m^2 - n^2 \end{bmatrix}, \quad \mathbf{R}_2 = \begin{bmatrix} m^2 & n^2 & 0 & 0 & 0 & mn \\ n^2 & m^2 & 0 & 0 & 0 & -mn \\ 0 & 0 & 1 & 0 & 0 & 0 \\ 0 & 0 & 0 & m & -n & 0 \\ 0 & 0 & 0 & n & m & 0 \\ -2mn & 2mn & 0 & 0 & 0 & m^2 - n^2 \end{bmatrix}, \tag{47}$$

with $m = \cos\theta$ and $n = \sin\theta$. The governing eigenvalue problem is then solved by using the rotated stiffness matrix in the constitutive relations $\boldsymbol{\sigma} = \mathbf{C}_\theta\boldsymbol{\varepsilon}$.

The results are shown in Fig. 4 in terms of phase velocity and group velocity. The latter result was computed from Eq. (36). Since an elastic material is being considered, the group velocity is now appropriate. Solutions were found for a wave propagation direction oriented at 0° (Figs. 4(a) and (b)), at 45° (Figs. 4(c) and (d)) and at 90° (Figs. 4(e) and (f)) with respect to the fiber direction 1. In the 45° case, the option of tracing the Lamb and the SH modes separately is no longer possible due to the coupling effects between them. This option is instead viable in the 0° and 90° propagation directions. For purposes of comparison, both Lamb and SH modes are shown in all plots of Fig. 4. That Lamb and SH modes are coupled in the 45° direction can be readily seen in Figs. 4(c) and (d) by noticing that the lowest-order SH_0 mode has some degree of dispersion. The same SH_0 mode is, instead, perfectly nondispersive in the 0° and 90° plots. It can also be seen that the velocity values for the Lamb modes tend to decrease with increasing wave propagation angle as expected, particularly for the symmetric modes. The results are coincident with those obtained in Ref. [23] by the SPBW method for the 0° and the 45° directions; this reference, however, did not report the SH modes in the 0° direction and the $\mathbf{A}_0$ mode in the 45° direction.

4.1.3. Viscoelastic orthotropic plate

The next example is a viscoelastic orthotropic plate that was examined in Ref. [20]. The plate is a 3.6-mm-thick carbon-epoxy with density $\rho = 1560\,\mathrm{kg/m^3}$. The elastic ($C_{ij}$) and viscoelastic ($\eta_{ij}$) properties are given in Table 2 in the principal directions of material symmetry. The hysteretic viscoelastic model was used here.

The results are shown in Fig. 5 in terms of phase velocity and attenuation for the symmetric modes (plots (a) and (b)) and for the antisymmetric modes (plots (c) and (d)), for a propagation direction at 60° from principal direction 1. Since damping is being considered, the solutions exist in the entire frequency range. When damping is small, the existence of solutions below the undamped cut-off frequencies has little effect on the phase velocity above these frequencies. Nevertheless, branches of the phase velocity curves that would be distinct in the undamped case may become connected in the damped case. An example of a branch connection is shown in the inset of Fig. 5(a) that zooms into the 800–820 kHz range. Similar branch connection phenomena were observed in damped isotropic plates [25,26].

It can also be clearly seen in Fig. 5 that the mode attenuation is strongly related to the phase velocity dispersion, with strong dispersion corresponding to rapidly changing attenuation. As the frequency tends to infinity, the modes converge to the bulk wave solutions. Accordingly, their attenuation becomes a linear function of the frequency.

The results are coincident with those obtained in Ref. [20] by the SPBW method. This reference, however, reports fewer modes than those presented in Fig. 5. In both Ref. [20] and the present work, the number of modes being shown is generally determined by the upper-bound threshold chosen for the attenuation values.

4.1.4. Elastic composite laminate

A quasi-isotropic composite laminate made of unidirectional T800/924 graphite-epoxy laminae with a stacking sequence of $[\pm 45/0/90]_S$ was considered next. Each lamina has a thickness of 0.125 mm resulting in a total laminate thickness of 1 mm. The elastic constants for the material were taken from Ref. [28]: $E_{11} = 161\,\mathrm{GPa}$, $E_{22} = 9.25\,\mathrm{GPa}$, $G_{12} = 6.0\,\mathrm{GPa}$, $\upsilon_{12} = 0.34$ and $\upsilon_{23} = 0.41$. The material density was $\rho = 1500\,\mathrm{kg/m^3}$. The corresponding terms of the stiffness matrix are shown in Table 3.

Two, quadratic mono-dimensional finite elements were used to model each of the eight laminae. Fig. 6 presents the phase and group velocity results for waves propagating along the fiber direction of the 0° lamina. The $\mathbf{C}$ matrices of each lamina were opportunely rotated according to Eq. (46). Also shown in Fig. 6 are the displacement cross-sectional shapes extracted from the SAFE analysis for modes $m1$, $m2$ and $m3$ at 800 kHz and $m4$, $m5$ and $m6$ at 1.6 MHz. The reference system is consistent with Fig. 1(a). It can be clearly seen that the mode shapes for a laminated composite are generally quite different from the analogous mode shapes of an isotropic homogeneous plate. Abrupt changes can occur at the interface between two laminae.

The mode shape predictions can be exploited in NDE/SHM applications to enhance the sensitivity to a particular structural defect and/or to minimize the losses due to leakage in the surrounding medium. For example, an internal defect would be most efficiently detected by a mode such as $m2$ in Fig. 6 with large

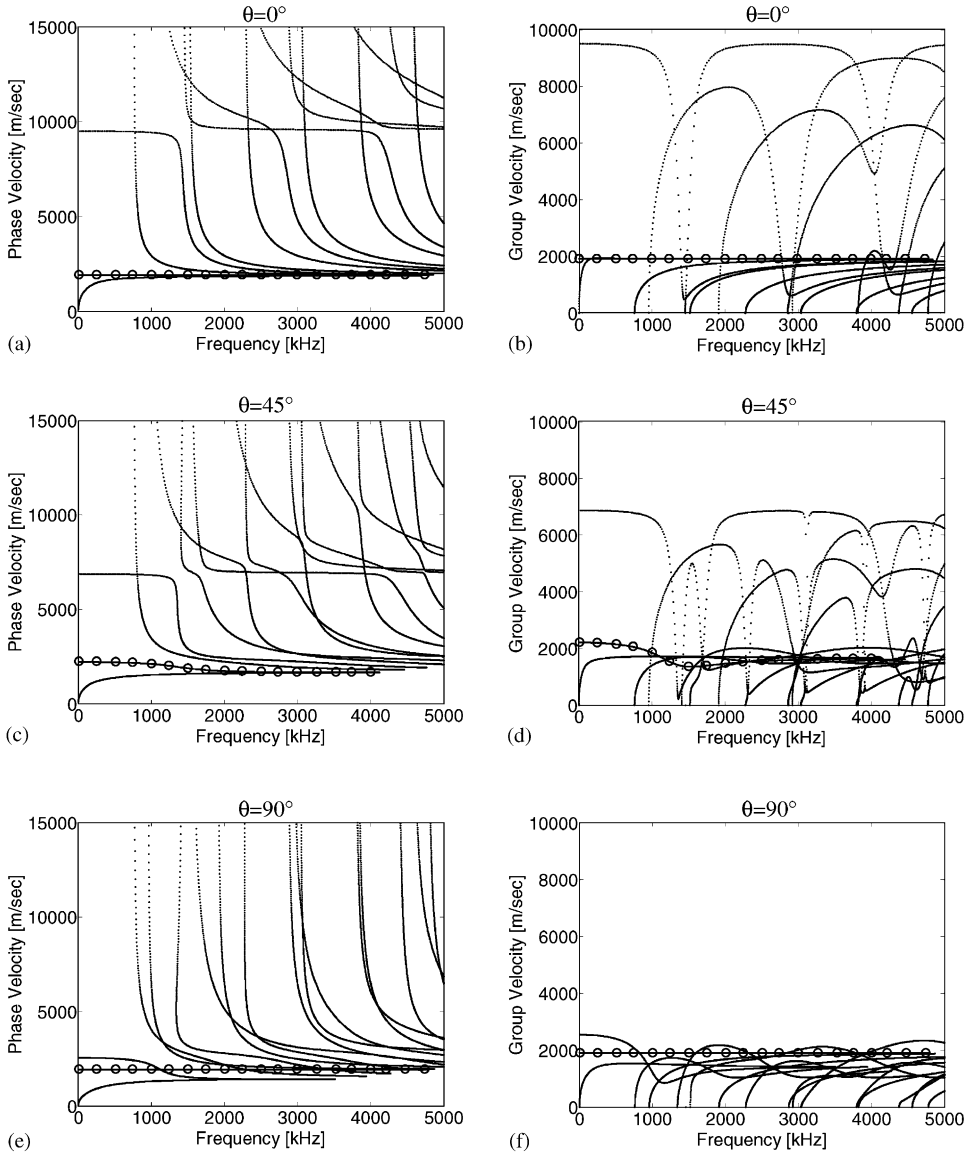

Fig. 4. Dispersion results for a 1 mm thick, elastic transversely isotropic carbon-epoxy laminate in vacuum: (a) phase velocity for waves propagating along principal direction 1, (b) group velocity for waves propagating along principal direction 1, (c) phase velocity for waves propagating at 45° from principal direction 1, (d) group velocity for waves propagating at 45° from principal direction 1, (e) phase velocity for waves propagating along principal direction 2, (f) group velocity for waves propagating along principal direction 2. –○–, SH_0 mode.

Table 2
Elastic and viscous properties of the orthotropic plate examined in Ref. [20] and in the present study (elastic constants in GPa; viscosities given at 2.0 MHz)

C_{11}	C_{12}	C_{13}	C_{22}	C_{23}	C_{33}	C_{44}	C_{55}	C_{66}
86.60	9.00	6.40	13.50	6.80	14.00	2.72	4.06	4.70
η_{11}	η_{12}	η_{13}	η_{22}	η_{23}	η_{33}	η_{44}	η_{55}	η_{66}
7.50	0.30	0.60	0.60	0.25	0.28	0.10	0.12	0.28

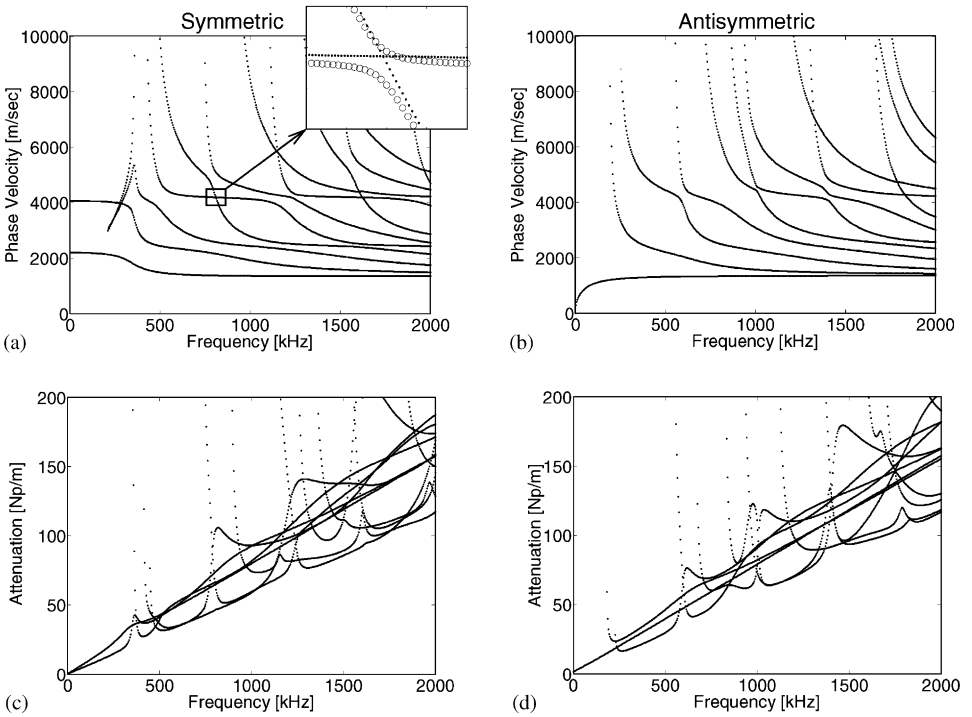

Fig. 5. Dispersion results for a 3.6 mm thick, viscoelastic orthotropic carbon-epoxy plate in vacuum for waves propagating at 60° from principal direction 1: (a) phase velocity for the symmetric modes (inset: ○○○○, undamped case; ……, damped case); (c) attenuation for the symmetric modes, (b) phase velocity for the antisymmetric modes, (d) attenuation for the antisymmetric modes.

Table 3
Elastic properties of the T800/924 lamina (elastic constants in GPa)

C_{11}	C_{12}	C_{13}	C_{22}	C_{23}	C_{33}	C_{44}	C_{55}	C_{66}
168.4	5.45	5.45	11.3	4.74	11.3	3.28	6.0	6.0

displacements at the laminate's mid-plane. Acoustic losses from leakage into a surrounding fluid medium would be severe for modes with large out-of-plane displacements at the laminate's surface such as $m1$ in Fig. 6. Clearly these trends will depend on the particular frequency used to probe the structure.

4.1.5. Viscoelastic orthotropic plate: comparison between hysteretic and Kelvin-Voigt models

In this section the viscoelastic orthotropic plate studied in Ref. [29] is examined. The plate is a unidirectional lamina of 1 mm in thickness. The material's properties are shown in Table 4. The viscosities are given at 2.242 MHz.

SAFE results were obtained for both the hysteretic and the Kelvin–Voigt viscoelastic models for the purpose of comparing the two solutions. Eqs. (3) and (4) were used to define the complex stiffness matrix in the two models, where $\overline{f}$ was set equal to 2.242 MHz in Eq. (3). Ten, quadratic mono-dimensional elements were used for the discretization. The wave propagation direction coincided with the fiber direction 1. Thus the Lamb and SH modes could be solved separately. Fig. 7 presents the Lamb wave results obtained by using the hysteretic model in the left column, and by using the Kelvin–Voigt model in the right column. Fig. 8 presents the corresponding plots for the SH modes. It can be seen in both figures that changing the viscoelastic model has little effect on the phase or the energy velocity results in the frequency range considered. Appreciable

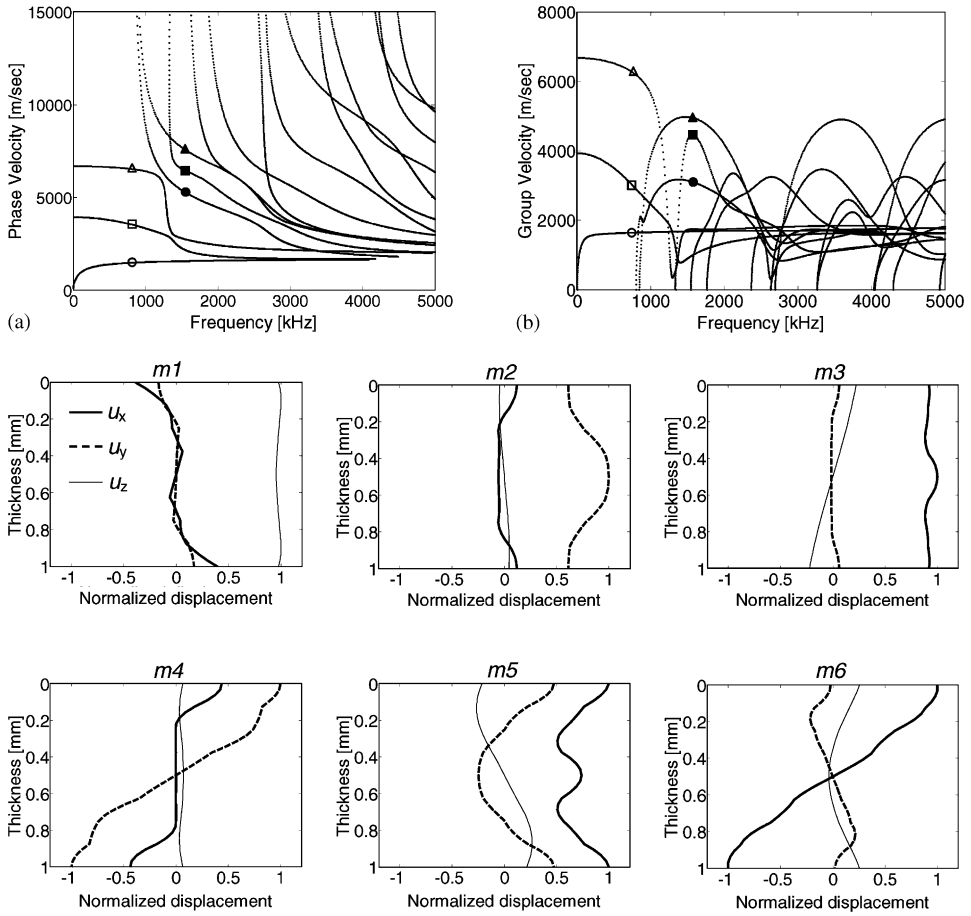

Fig. 6. Dispersion results for a 1 mm thick, elastic $[\pm 45/0/90]_S$ composite laminate in vacuum for waves propagating along principal direction 1 of the 0° lamina: (a) phase velocity, (b) group velocity. Cross-sectional displacement mode shapes shown for: ○, mode $m1$; □, mode $m2$; △, mode $m3$; ●, mode $m4$; ■, mode $m5$; ▲, mode $m6$.

Table 4
Elastic and viscous properties of the orthotropic plate examined in Ref. [29] and in the present study (elastic constants in GPa; viscosities given at 2.242 MHz)

C_{11}	C_{12}	C_{22}	C_{13}	C_{23}	C_{33}	C_{44}	C_{55}	C_{66}
132	6.9	5.9	12.3	5.5	12.1	3.32	6.21	6.15
η_{11}	η_{12}	η_{13}	η_{22}	η_{23}	η_{33}	η_{44}	η_{55}	η_{66}
0.40	0.001	0.016	0.037	0.021	0.043	0.009	0.015	0.02

effects are instead seen in the attenuation plots (Figs. 7(e) and (f) and 8(e) and (f)). In particular, both models give the same solution at the characterization frequency of 2.242 MHz as expected. Above and below this frequency, the Kelvin–Voigt model results in respectively larger and smaller attenuation values compared to the hysteretic model.

4.1.6. Composite-to-composite adhesively bonded joint

This section presents SAFE results relative to ongoing efforts at UCSD aimed at the development of an on-board SHM system for Unmanned Aerial Vehicles (UAVs) based on integrated sensors and ultrasonic guided

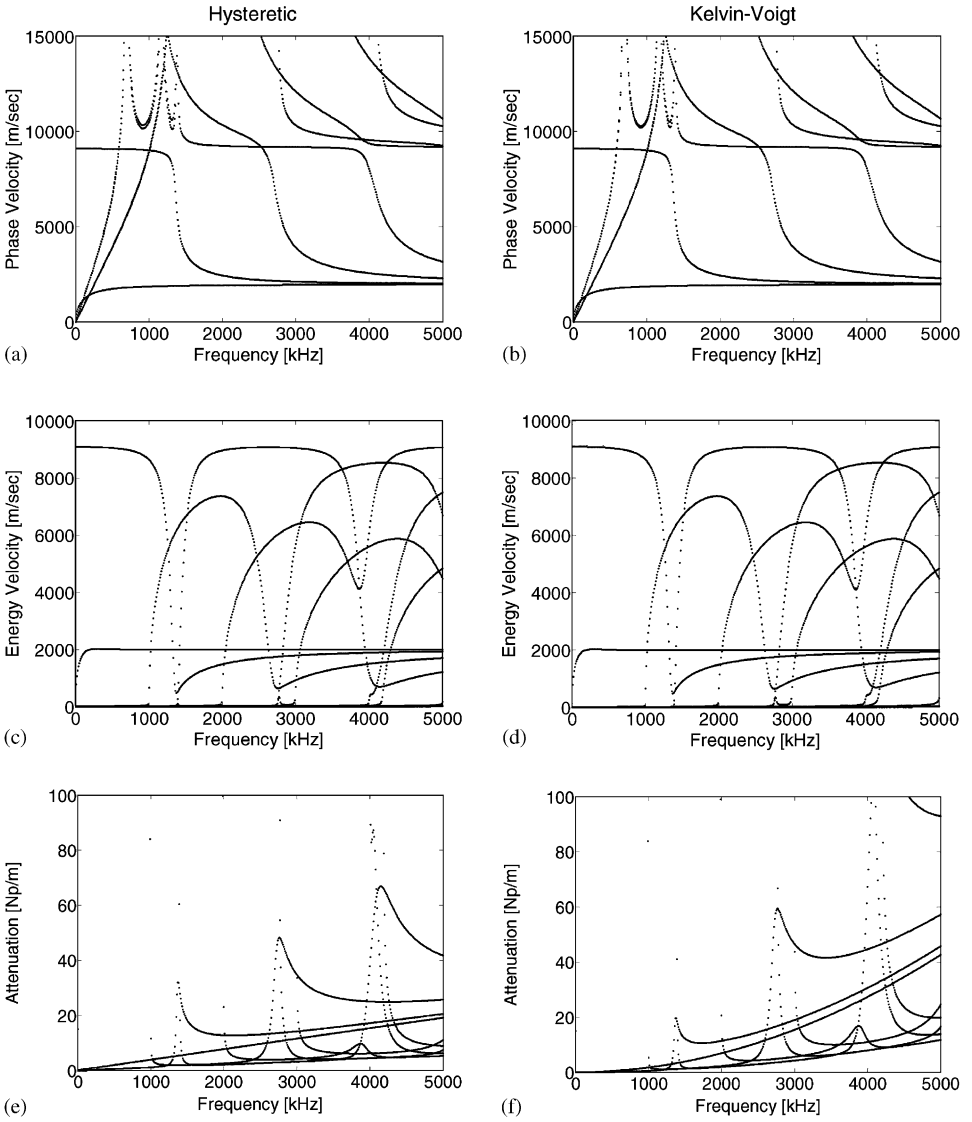

Fig. 7. Dispersion results (Lamb modes) for a 1 mm thick, viscoelastic orthotropic plate in vacuum: (a), (c), (e) case of hysteretic viscoelastic model; (b), (d), (f) case of Kelvin–Voigt viscoelastic model.

waves [30]. The monitoring is being targeted to the adhesive bond between the UAV composite wing skin and the tubular composite spar shown in the drawing of Fig. 9. The spar runs along the lengthwise direction of the wing.

The wing skin under investigation is a T300/5208 carbon-epoxy laminate with a stacking sequence $[0/\pm 45/0]_S$ and a thickness of 0.133 mm per lamina. The 0° direction is parallel to the spar lengthwise direction. The wing skin was modeled by the usual rotation of the stiffness matrix according to Eq. (46). The spar is a cross-ply tubular section made of T800/924 and having a total wall thickness of 5.235 mm. In the model, the spar was considered as one equivalent viscoelastic orthotropic layer without loss of accuracy [30]. The adhesive layer had a typical thickness of 0.203 mm. One quadratic element was used for each lamina of the skin and for the bond layer, whereas five elements were used for the spar wall. The hysteretic viscoelastic model was used for each of the components.

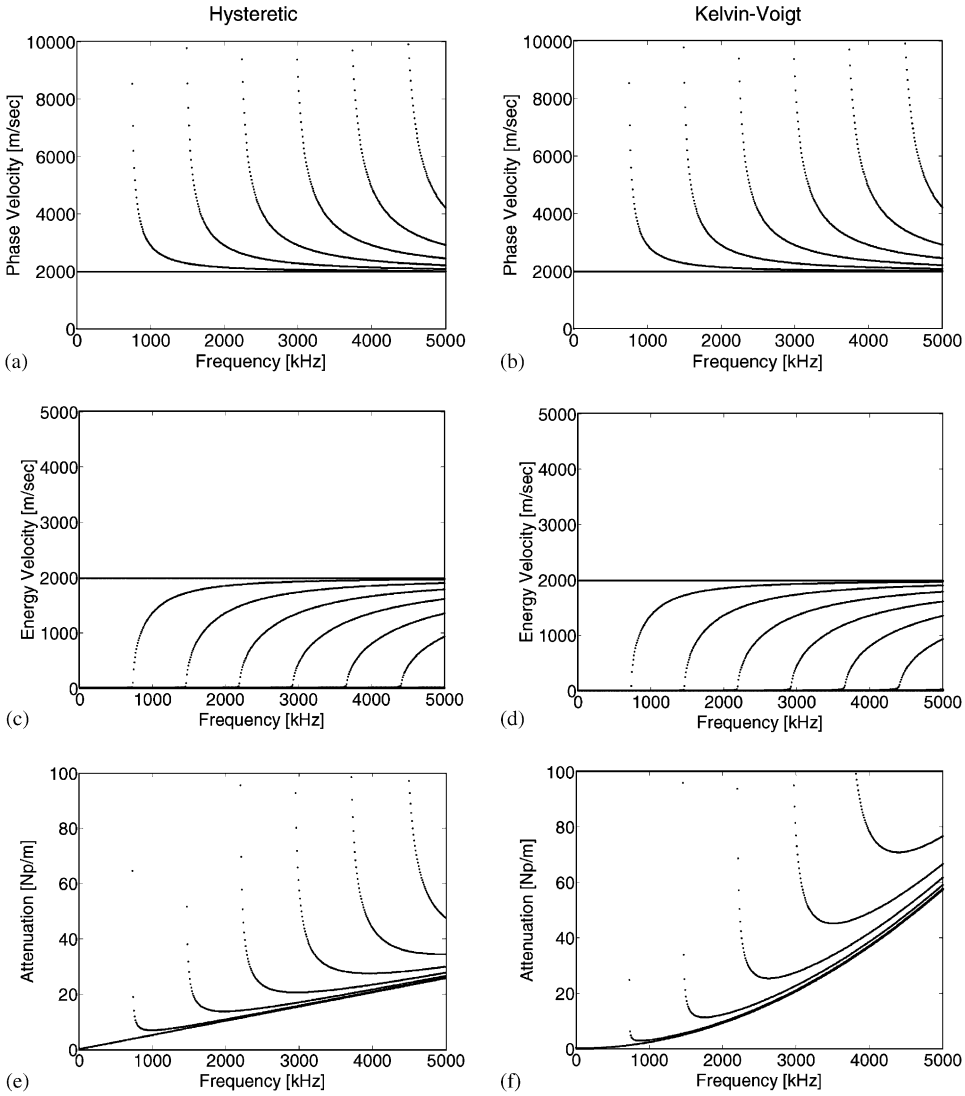

Fig. 8. Dispersion results (SH modes) for a 1 mm thick, viscoelastic orthotropic plate in vacuum: (a), (c), (e) case of hysteretic viscoelastic model; (b), (d), (f) case of Kelvin–Voigt viscoelastic model.

The on-board sensor disposition is such that the wave is generated and detected on the wing skin on either side of the joint. The wave propagation direction is perpendicular to the spar, along direction x in the drawing of Fig. 9. Any degradation in the bond condition can then be monitored by measuring changes in the strength of the ultrasonic transmission through the joint.

SAFE dispersion results are presented in Fig. 9 for the disbonded skin-to-spar interface, the most extreme bond degradation that was considered in this study. The specific material properties assumed for the various layers of the joint are summarized in Table 5. Densities were 1530 kg/m^3 for the skin and the spar, and 1421 kg/m^3 for the adhesive layer. Table 6 compares the ultrasonic properties assumed for the disbonded layer to those assumed for the regular adhesive layer. It can be seen that the largest degradation was imposed to the shear wave velocity to reflect the inability of the disbond to transfer shear stresses.

The weak properties of the disbonded interface essentially de-couple the dispersive behavior of the wing skin from that of the spar. Accordingly, the solutions in Fig. 9 show modes whose energy is mainly concentrated within the wing skin above the bondline (identified in the figure by $S_{0,plate}$, $A_{0,plate}$, $SH_{0,plate}$, etc.), and modes whose energy is mainly concentrated within the spar below the bondline (identified by $S_{0,spar}$, $A_{0,spar}$, $SH_{0,spar}$,

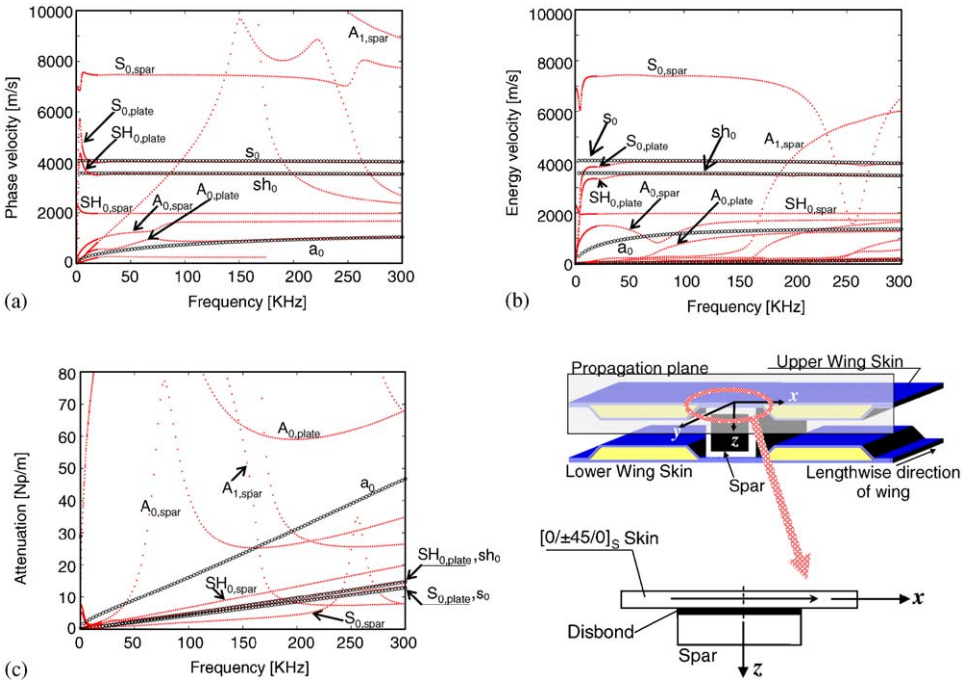

Fig. 9. Dispersion results for UAV wing skin-to-spar adhesive joint with a disbonded interface for waves propagating perpendicularly to the spar lengthwise direction: (a) phase velocity, (b) energy velocity, (c) attenuation. ○○○○, single skin modes.

Table 5
Elastic and viscous properties for the UAV wing skin-to-spar joint (elastic constants in GPa. *from Ref. [31])

Layer	C'_{11} (C''_{11})	C'_{12} (C''_{12})	C'_{13} (C''_{13})	C'_{22} (C''_{22})	C'_{23} (C''_{23})	C'_{33} (C''_{33})	C'_{44} (C''_{44})	C'_{55} (C''_{55})	C'_{66} (C''_{66})
Wing skin lamina	135 (8.23)*	5.70 (0.65)*	5.70 (0.60)*	14.2 (0.34)*	8.51 (0.25)*	14.2 (0.65)*	2.87 (0.24)*	4.55 (0.28)*	4.55 (0.25)*
Spar wall	88.0 (4.28)	5.45 (0.65)	5.09 (0.425)	88.0 (4.28)	5.09 (0.425)	11.3 (0.65)	4.64 (0.26)	4.64 (0.26)	6.00 (0.25)
Disbond	0.070 (0.035)	0.069 (0.035)	0.069 (0.035)	0.070 (0.035)	0.069 (0.035)	0.070 (0.035)	0.00012 (0.00013)	0.00012 (0.00013)	0.00012 (0.00013)

Table 6
Bulk ultrasonic velocities and attenuations of the UAV wing skin-to-spar interface layer

Layer	c_L (m/s)	c_T (m/s)	κ_L (Np/λ)	κ_T (Np/λ)
Regular bond	2410	1210	0.149	0.276
Disbond	241	12.1	1.497	2.763

etc.). The former modes closely match those that would be supported by the wing skin alone (identified by s_0, a_0, sh_0 and represented by open dots in Fig. 9). The match between the "*skin*" modes of the disbonded joint and the pure single-skin modes becomes closer as the frequency increases (compare, for example, $A_{0,plate}$ and a_0). One implication is that waves generated on the wing skin outside of the joint will be transferred very

efficiently across the disbonded interface through one of the "skin" modes. Consequently, the occurrence of a disbond can be detected by an increased strength of ultrasonic transmission compared to a regularly bonded joint.

4.2. Arbitrary cross-sections: viscoelastic railroad track

The purpose of this section is to demonstrate the applicability of the SAFE approach to waveguides of arbitrary cross-sections that cannot be solved by exact methods. The case treated is that of a railroad track. Knowledge of the dispersive behavior of guided waves in rails is relevant for the purpose of train noise reductions at low frequencies, below 6 kHz [32], and for long-range NDE defect detection at high frequencies, up to 50 kHz [33,34].

The rail considered is a typical 115-lb A.R.E.M.A. section, modeled as an isotropic material with hysteretic damping, and having the following properties: $\rho = 7932\,\mathrm{kg/m^3}$, $c_L = 5960\,\mathrm{m/s}$, $c_T = 3260\,\mathrm{m/s}$, $\kappa_L = 0.003\,\mathrm{Np/wavelength}$ and $\kappa_T = 0.043\,\mathrm{Np/wavelength}$. The rail cross-section has a complex geometry with one vertical axis of symmetry. The mesh, shown in Fig. 10 and generated by Matlab's "pdetool," used 81 nodes for 106 triangular elements with linear interpolation displacement functions. Compared to the plate systems, a compromise was made by decreasing the order of the interpolation function with the increased number of dof necessary to move from a 1-D discretization to the bi-dimensional discretization of the rail track.

The dispersion results are shown in Fig. 10 up to a frequency of 50 kHz. The complexity of the modes is evident in these plots. Notice that no prior solutions for the attenuation values are available from the literature in this frequency range, since previous wave propagation models of rails did not include damping, with the exception of low-frequency (< 6 kHz) studies [35,36]. Knowledge of the high-frequency attenuation, however, is important to identify low-loss mode-frequency combinations that can provide truly long-range defect detection. A zoom into the low-frequency phase velocity curves is shown in Fig. 11 along with the first five

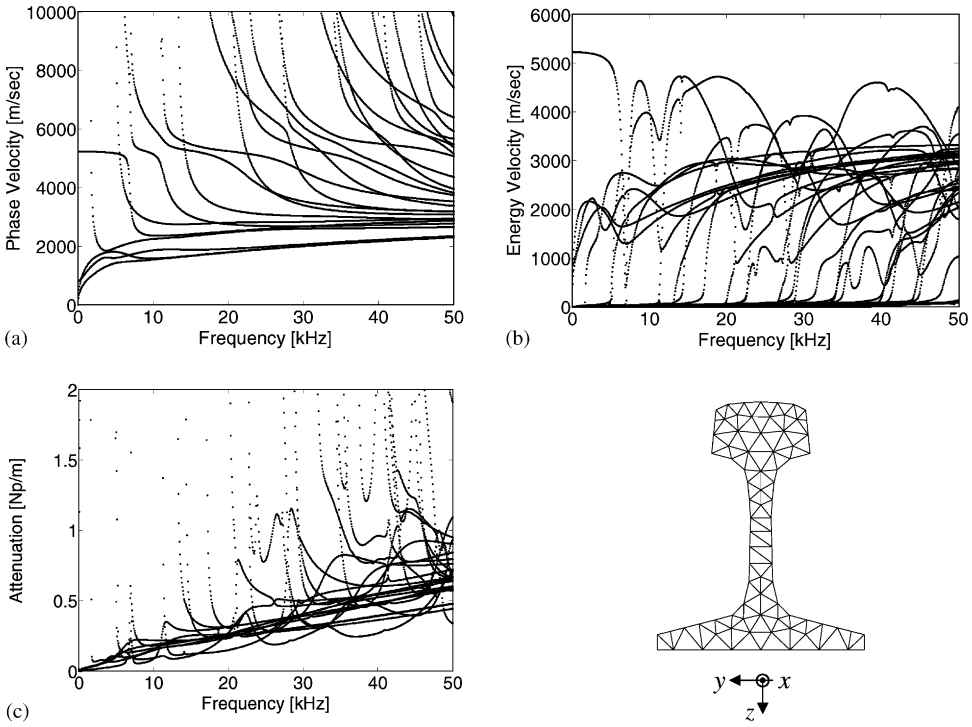

Fig. 10. Dispersion results for a 115-lb A.R.E.M.A., viscoelastic rail for waves propagating along the rail running direction: (a) phase velocity, (b) energy velocity, (c) attenuation.

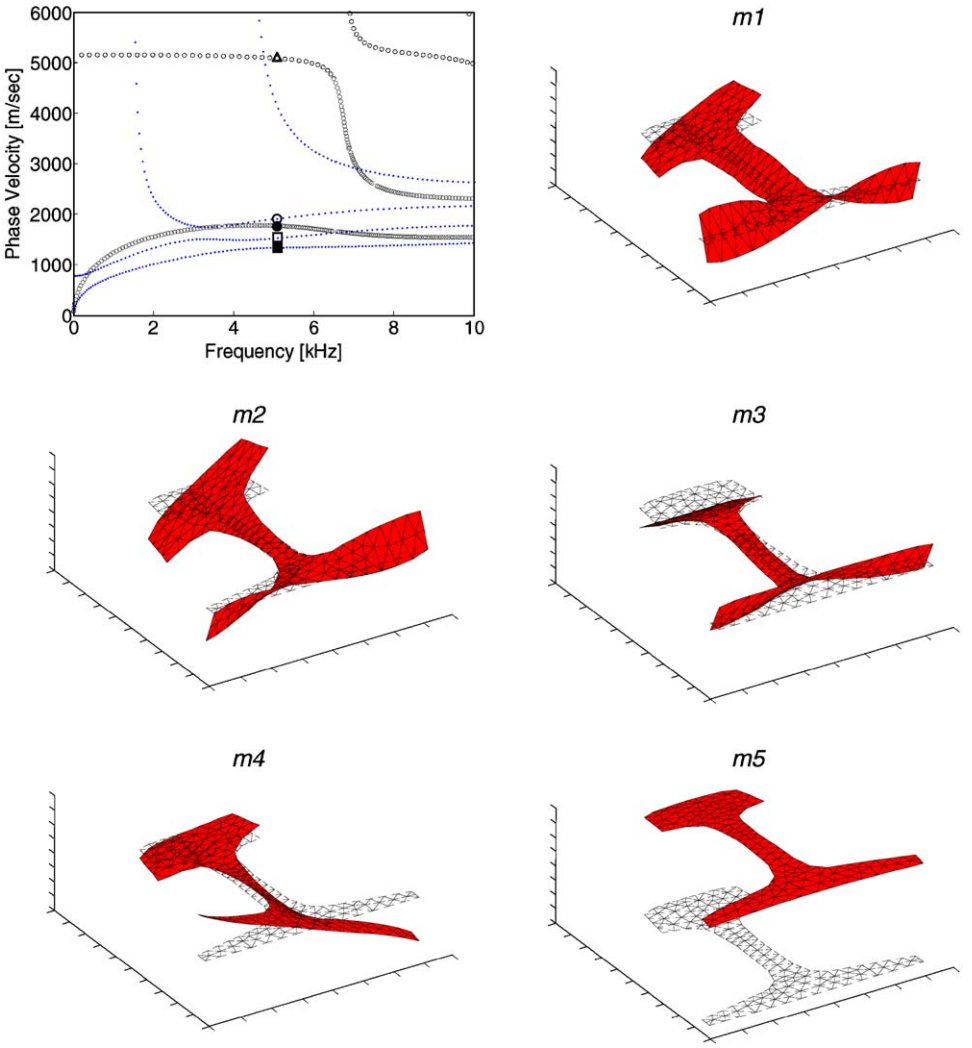

Fig. 11. Dispersion results for a 115-lb A.R.E.M.A., viscoelastic rail: phase velocity for frequencies below 10 kHz, and first five cross-sectional mode shapes at 5 kHz. ■, mode $m1$; □, mode $m2$; ●, mode $m3$; ○, mode $m4$; △, mode $m5$; ○○○○, symmetric modes; ……, antisymmetric modes.

cross-sectional mode shapes at 5 kHz. It can be seen that modes $m1$, $m2$ and $m4$ are antisymmetric with respect to the x–z plane, while modes $m3$ and $m5$ are symmetric. It can also be seen that some of the modes excite preferably a certain portion of the rail, whether the head or the base. This information can be used in practical NDE tests to target defects at various locations in the rail section. Similarly, knowledge of the mode shapes is necessary to design the appropriate wave excitation/detection approach.

5. Discussion and conclusions

In this paper a general SAFE method was proposed and derived for modeling wave propagation in waveguides of generally arbitrary cross-sections. The main innovation over SAFE models proposed in the past is accounting for viscoelastic material damping, and thus representing the energy velocity and the attenuation curves. The hysteretic viscoelastic model (frequency independent) and the Kelvin–Voigt viscoelastic model (frequency dependent) were used in the formulation. The energy velocity values (for damped waveguides) and the group velocity values (for undamped waveguides) are obtained at each individual wavenumber–frequency solution, without the need for tracking the modes and without considering adjacent solutions in finite

difference calculations. The knowledge of the dispersive wave properties is relevant for NDE/SHM testing for identifying propagating modes, locating defects, as well as exciting low-loss mode-frequency combinations for increased ranges.

The method was validated on various examples, some of which were examined previously by SPBW methods. The examples included viscoelastic orthotropic plates, laminated composite plates, composite-to-composite adhesive bonds in UAV wings, and railroad tracks.

The approximation of any SAFE method depends only on the discretization of the waveguide's cross-section. In the absence of rigorous convergence criteria, the rule of thumb should be having the necessary number of elements to properly represent the cross-sectional mode shapes of the problem for the highest frequency of interest.

The solutions of the SAFE eigenvalue problem are the displacement components. Consequently, if strain and stress components are of interest, the mesh should be refined further to compensate for the loss of accuracy of the differentiation process. This aspect is also important in the evaluation of the energy velocity. Energy velocity is, in fact, a function of the Poynting vector, Eq. (37), thus, in turn, is a function of the stress and the displacement derivatives, Eq. (38). Thus the accuracy of the energy velocity solutions depends on the accuracy of the displacement derivatives. Alternatively, the group velocity is a function of the displacement eigenvectors, Eq. (36). In summary, the phase velocity, the group velocity and the attenuation curves are calculated with the same order of accuracy, while the energy velocity curves require a more refined discretization to achieve the same accuracy.

Acknowledgments

Funding for this project was provided by the UCSD/Los Alamos Laboratory Cooperative Agreement for Research and Education (CARE), by the US National Science Foundation Grant #0221707, and by the US Federal Railroad Administration Grant #DTFR53-02-G-00011. Funding was also provided by the Italian Ministry for University and Scientific&Technological Research MIUR (40%). The topic treated is one of the research thrusts of the Centre of Study and Research for the Identification of Materials and Structures (CIMEST).

References

[1] M.J.S. Lowe, Matrix techniques for modeling ultrasonic waves in multilayered media, *IEEE Transactions on Ultrasonics, Ferroelectrics, and Frequency Control* 42 (1995) 525–542.

[2] P.E. Lagasse, Higher-order finite element analysis of topographic guides supporting elastic surface waves, *Journal of the Acoustical Society of America* 53 (1973) 1116–1122.

[3] B. Aalami, Waves in prismatic guides of arbitrary cross section, *Journal of Applied Mechanics* 40 (1973) 1067–1072.

[4] K.H. Huang, S.B. Dong, Propagating waves and edge vibrations in anisotropic composite cylinders, *Journal of Sound and Vibration* 96 (1984) 363–379.

[5] L. Gavrić, Finite element computation of dispersion properties of thin-walled waveguides, *Journal of Sound and Vibration* 173 (1994) 113–124.

[6] L. Gavrić, Computation of propagating waves in free rail using a finite element technique, *Journal of Sound and Vibration* 185 (1995) 531–543.

[7] A.C. Hladky-Hennion, Finite element analysis of the propagation of acoustic waves in waveguides, *Journal of Sound and Vibration* 194 (1996) 119–136.

[8] P. Wilcox, M. Evans, O. Diligent, M.J.S. Lowe, P. Cawley, Dispersion and excitability of guided acoustic waves in isotropic beams with arbitrary cross section, *Review of Progress in Quantitative NDE* 21 (2002) 203–210.

[9] A.C. Hladky-Hennion, P. Langlet, M. de Billy, Finite element analysis of the propagation of acoustic waves along waveguides immersed in water, *Journal of Sound and Vibration* 200 (1996) 519–530.

[10] V.V. Volovoi, D.H. Hodges, V.L. Berdichevsky, V.G. Sutyrin, Dynamic dispersion curves for non-homogeneous, anisotropic beams with cross-section of arbitrary geometry, *Journal of Sound and Vibration* 215 (1998) 1101–1120.

[11] T. Hayashi, W.J. Song, J.L. Rose, Guided wave dispersion curves for a bar with an arbitrary cross-section, a rod and rail example, *Ultrasonics* 41 (2003) 175–183.

[12] O. Onipede, S.B. Dong, Propagating waves and end modes in pretwisted beams, *Journal of Sound and Vibration* 195 (1996) 313–330.

[13] H. Taweel, S.B. Dong, M. Kazic, Wave reflection from the free end of a cylinder with an arbitraty cross-section, *International Journal of Solids and Structures* 37 (2000) 1701–1726.

[14] S. Finnveden, Evaluation of modal density and group velocity by a finite element method, *Journal of Sound and Vibration* 273 (2004) 51–75.
[15] S.B. Dong, K.H. Huang, Edge vibrations in laminated composite plates, *Journal of Applied Mechanics* 52 (1985) 433–438.
[16] O.M. Mukdadi, Y.M. Desai, S.K. Datta, A.H. Shah, A.J. Niklasson, Elastic guided waves in a layered plate with rectangular cross section, *Journal of the Acoustical Society of America* 112 (2002) 1766–1779.
[17] O.M. Mukdadi, S.K. Datta, Transient ultrasonic guided waves in layered plates with rectangular cross section, *Journal of Applied Physics* 93 (2003) 9360–9370.
[18] P.J. Shorter, Wave propagation and damping in linear viscoelastic laminates, *Journal of the Acoustical Society of America* 115 (2004) 1917–1925.
[19] F. Birgersson, S. Finnveden, C.-M. Nilsson, A spectral super element for modelling of plate vibration—part 1: general theory, *Journal of Sound and Vibration* 287 (2005) 297–314.
[20] G. Neau, *Lamb Waves in Anisotropic Viscoelastic Plates. Study of the Wave Fronts and Attenuation,*, PhD Thesis, L'Université Bordeaux I, 2003.
[21] J.L. Rose, *Ultrasonic Waves in Solid Media*, Cambridge University Press, Cambridge, 1999.
[22] *Matlab 7.04: User's Guide,*, The Mathworks, Natick, MA, 2000.
[23] B.N. Pavlakovic, M.J.S. Lowe, D.N. Alleyne, P. Cawley, Disperse: a general purpose program for creating dispersion curves, *Review of Progress in Quantitative NDE* 16 (1997) 185–192.
[24] X. Han, G.R. Liu, Z.C. Xi, K.Y. Lam, Characteristics of waves in a functionally graded cylinder, *International Journal for Numerical Methods in Engineering* 53 (2002) 653–676.
[25] A. Bernard, M.J.S. Lowe, M. Deschamps, Guided waves energy velocity in absorbing and non-absorbing plates, *Journal of the Acoustical Society of America* 110 (2001) 186–196.
[26] A. Bernard, M. Deschamps, M.J.S. Lowe, Energy velocity and group velocity for guided waves propagating within an absorbing or non-absorbing plate in vacuum, *Review of Progress in Quantitative NDE* 18 (1999) 183–190.
[27] B.A. Auld, *Acoustic Fields and Waves in Solids (*twovolumes*)*, Krieger Publishing Company, Malabar, FL, 1990.
[28] B. Pavlakovic, M. Lowe, *Disperse User's Manual*, Imperial College London, London, UK, 2003.
[29] M. Deschamps, B. Hosten, The effects of viscoelasticity on the reflection and transmission of ultrasonic guided waves by orthotropic plate, *Journal of the Acoustic Society of America* 91 (1992) 2007–2015.
[30] H. Matt, I. Bartoli, F. Lanza di Scalea, Ultrasonic guided wave monitoring of composite wing skin-to-spar bonded joints in aerospace structures, *Journal of the Acoustic Society of America* 118 (2005) 2240–2252.
[31] G. Neau, M.J.S. Lowe, M. Deschamps, Propagation of lamb waves in anisotropic and absorbing plates: theoretical derivation and experiments, *Review of Progress in Quantitative NDE* 21 (2002) 1062–1069.
[32] D.J. Thompson, Wheel-rail noise generation—part III: rail vibration, *Journal of Sound and Vibration* 161 (2003) 421–446.
[33] P. Wilcox, M. Evans, B. Pavlakovic, D. Alleyne, K. Vine, P. Cawley, M.J.S. Lowe, Guided wave testing of rail, *Insight—NDT & Condition Monitoring* 45 (2003) 413–420.
[34] F. Lanza di Scalea, J. McNamara, Ultrasonic NDE of railroad tracks: air-coupled cross-sectional inspection and long-range inspection, *Insight—NDT & Condition Monitoring* 45 (2003) 394–401.
[35] T.X. Wu, D.J. Thompson, Analysis of lateral vibration behavior of railway track at high frequencies using a continuously supported multiple beam model, *Journal of the Acoustic Society of America* 106 (1999) 1369–1376.
[36] T.X. Wu, D.J. Thompson, A double Timoshenko beam model for vertical vibration analysis of railway track at high frequencies, *Journal of Sound and Vibration* 224 (1999) 329–348.